Düzce University Journal of Science & Technology, 13 (2025) 616-630

Düzce University
Journal of Science & Technology

Research Article

Enhanced Optical Coherence Tomography (OCT) of Prostate Nerves Through Integrated Image-Processing Techniques

Şükran YAMAN ATCI [a,*]
[a] *Department of Computer Programming , Vocational School, Haliç University, İstanbul, TURKEY*
* *Corresponding author's e-mail address: sukranatci@halic.edu.tr*
DOI: 10.29130/dubited.1547459

ABSTRACT

Cavernous nerves, located along the prostate gland's surface, are integral to erectile functionality. These nerves are at risk of injury during the surgical removal of a cancerous prostate gland. This research applies a suite of image processing algorithms—segmentation, denoising, and edge detection—to time-domain optical coherence tomography (OCT) images of prostates from different datasets of to improve the detection of cavernous nerves. Initially, the prostate OCT images are segmented to isolate the cavernous nerves from the adjacent glandular tissue. This is followed by the application of a locally adaptive denoising process using a dual-tree complex wavelet transform, aimed at reducing speckle noise. Subsequently, edge detection techniques are employed to enhance the imaging depth of the prostate gland. The combined application of these image processing techniques significantly improves the signal-to-noise ratio and imaging depth, enabling the automated identification of cavernous nerves. This enhanced imaging capability is crucial for supporting nerve-sparing approaches in laparoscopic and robotic prostate cancer surgeries.

Keywords: *OCT, Prostatic Tissue, Segmentation, Denoising, Edge Detection , Oncology Diagnostics*

Entegre Görüntü İşleme Teknikleri Sayesinde Prostat Sinirlerinin Geliştirilmiş Optik Koherens Tomografisi (OCT)

Öz

Kavernöz sinirler, prostat bezinin yüzeyi boyunca yer almaktadır ve erektil işlev için hayati öneme sahiptirler. Bu sinirler, kanserli bir prostat bezinin cerrahi olarak çıkarılması sırasında hasar görme riski taşımaktadır. Bu araştırma, kavernöz sinirlerin tanımlanmasını geliştirmek amacıyla, fare prostatlarındaki zaman alanı optik koherans tomografi (OCT) görüntülerine görüntü işleme algoritmaları—segmentasyon, gürültü azaltma ve kenar belirleme—uygulamaktadır. Başlangıçta, prostat OCT görüntüleri, kavernöz sinirleri çevreleyen bez dokusundan ayırmak için segmente edilir. Bunu, speckle gürültüsünü azaltmaya yönelik çift ağaç karmaşık dalga dönüşümüne dayalı yerel olarak uyarlanabilir bir gürültü azaltma işlemi takip eder. Ardından, prostat bezinin daha derinlerinin görüntülenmesini sağlamak için kenar belirleme teknikleri uygulanır. Bu görüntü işleme tekniklerinin birleşik uygulaması, sinyal-gürültü oranını ve görüntüleme derinliğini önemli ölçüde artırır ve kavernöz sinirlerin otomatik olarak tanımlanmasını sağlar. Bu gelişmiş görüntüleme yeteneği, laparoskopik ve robotik prostat kanseri ameliyatlarında sinir koruyucu yaklaşımları desteklemek için hayati öneme sahiptir.

Anahtar Kelimeler: *OCT Görüntüleme, Prostat Dokusu, Segmentasyon, Gürültü Giderme, Kenar Algılama , Onkoloji Teşhisi*

Received: 12/09/2024, Revised: 05/10/2024, Accepted: 17/12/2024

I.INTRODUCTION

The safeguarding of cavernous nerves during radical prostatectomy is crucial for the retention of function after surgery. Due to their close proximity to the surface of the prostate, these nerves are prone to injury during the excision of the cancerous prostate gland. Their minute size and the variable trajectory across patients add complexity to accurately mapping their course, which is essential for effective surgical outcomes. Such factors likely contribute to the broad range of postoperative potency rates, reported as varying between 9 and 86% following prostate cancer surgeries [1]. Consequently, technological advancements that enhance cavernous nerves' detection, imaging, and visualization could significantly bolster nerve conservation efforts and, by extension, postoperative functionality.

Prostate tissue is composed of both glandular and connective tissues. Within whole slide images (WSI), glands appear as hollow, white structures, often exhibiting a branched morphology. This glandular appearance underpins the Gleason grading system, which is used to assess the severity of prostate cancer given in Figure 1a and b. The Gleason grading system is a histopathological classification method widely used to evaluate the aggressiveness of prostate cancer based on glandular architectural patterns observed under a microscope. It assigns a primary and secondary grade, each ranging from 1 to 5, reflecting the most and second-most predominant tumor patterns, respectively, with the sum (Gleason score) ranging from 2 to 10, which correlates with tumor differentiation and clinical outcomes[2,3]. Lower scores (e.g., 2-4) are associated with well-differentiated, less aggressive tumors, whereas higher scores (e.g., 8-10) indicate poorly differentiated, highly aggressive cancers with a worse prognosis, underscoring its significance in guiding therapeutic decision-making and prognostication in clinical practice [2]. Optical Coherence Tomography (OCT) represents a non-invasive imaging modality that offers high-resolution, cross-sectional views of microstructures within biological tissues in vivo and in situ [2]. Although recent studies have successfully applied OCT to visualize cavernous nerves within human prostates [4,5], there is a recognized need for further enhancements in OCT image quality to facilitate the nerves' identification before it can be adopted clinically [5]. Recent advancements have further highlighted the potential of OCT in prostate imaging, with studies focusing on improving resolution and image processing techniques for better glandular and connective tissue differentiation [8,9]. Moreover, emerging applications of OCT in identifying microstructural changes linked to cancer progression have been reported, demonstrating its capability to complement traditional histopathological assessments [16] with efforts to enhance nerve visualization through machine learning algorithms integrated with OCT [17], paving the way for its broader clinical adoption. Additionally, recent comparative studies have explored the role of OCT in distinguishing benign from malignant lesions, revealing its potential as an adjunct diagnostic tool [18]. Finally, advances in OCT hardware have achieved greater imaging depth and clarity, which may significantly impact its utility in intraoperative prostate cancer management [19].

Another study that used a data schema and flow to inspire this study, OCT images were procured in vivo via a clinical endoscopic OCT apparatus (Imalux, Cleveland, Ohio) that integrates a single-mode fiber common-path interferometer-based scanning mechanism [1]). The imaging was facilitated by a probe with 2.6-mm outer diameter, enabling the capture of real-time images at a resolution of 200x200 pixels, with axial and lateral resolutions of 11 microns and 25 microns, respectively.

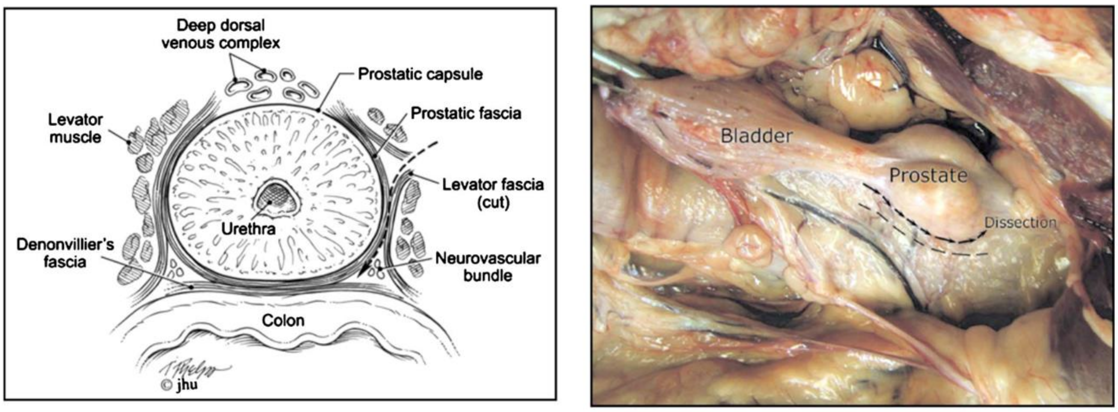

Figure 1 (a). *Cross-sectional illustration of the human prostate, depicting the position of the neurovascular bundles adjacent to the prostate surface, illustrated from Rassweiler et al. (2006)* [6]. *With the* ***(b)*** *the dashed line marks the dissection pathway between the prostatic capsule and the neurovascular bundle.*

For that persfective, this study delineates a structured method incorporating three synergistic image processing algorithms to enhance the visualization and identification of cavernous nerves within prostate OCT imagery. Earlier studies have applied a segmentation strategy effectively for recognizing cavernous nerves [15]. For this purpose, open-sourced databases named Prostate cANcer graDe Assessment (PANDA-1 and PANDA-2) dataset [7, 15, 19] are utilized, comprising 160 OCT frames. It is noteworthy that the PANDA-2 dataset encompasses much more complex frames than its predecessor, PANDA-1, enhancing the robustness and depth of analysis possible. Nonetheless, imaging the deeper structures of the prostate has remained a formidable challenge using OCT technologies. To address this, the initial segmentation strategy depicted in the left branch of Figure 1 is supplemented with denoising and edge detection techniques detailed in the right branch of the same figure. This advancement allows for a more nuanced understanding of prostate tissue variations and complexities captured in the PANDA-2 dataset.

Subsequent analysis demonstrates that the integration of the edge detection system significantly augments the capacity of OCT to image deeper prostate tissue structures, thus potentially enhancing diagnostic capabilities and surgical outcomes in prostate cancer treatments [10, 11]. In Figure 2, two-dimensional (2-D) OCT images of prostate tissues undergo segmentation to delineate the cavernous nerves from the adjacent glandular structures of the prostate. This segmentation process is critical for identifying and preserving these nerves during surgical procedures. Furthermore, the figure illustrates grading structural variations of prostate glands, systematically categorized into escalating levels from A to D, visually representing the progressive anatomical changes associated with different stages of prostate pathology. This study has shown that, despite limitations in reporting results from external hospitals, the use of stain normalization during processing significantly differentiates the distribution of predicted patches between malignant and normal cases, thereby validating the effectiveness of this methodology.

All microphotographs presented are stained with hematoxylin and eosin and captured at 5x lens magnification. This staining and magnification technique enables a detailed examination of cellular and structural anomalies, which are indicative of various stages in the progression of the prostate.

- **Benign Prostate Glands with Folded Epithelium (level A):** Characterized by pale cytoplasm and small, regular nuclei, these glands are closely clustered. Their structural integrity represents the healthiest form of prostate tissue, as assessed by histopathological standards.
- **Prostatic Adenocarcinoma, Gleason Pattern 3 (level B):** This pattern indicates no significant loss of glandular differentiation. Small, infiltrative glands intersperse among benign glands, featuring darker cytoplasm and enlarged nuclei with pronounced nucleoli and dark chromatin. Each glandular unit remains distinct and maintains a lumen, consistent with a lower-grade malignancy.

- **Prostatic Adenocarcinoma, Gleason Pattern 4 (level C):** Exhibiting partial loss of glandular differentiation, this pattern shows an incomplete formation of lumina. The microphotograph reveals irregular cribriform structures—epithelial sheets punctuated by multiple lumina. Additionally, there are both poorly formed small glands and some that are fused, all characteristic of Gleason Pattern 4.
- **Prostatic Adenocarcinoma, Gleason Pattern 5 (level D):** This highest grade is marked by an almost complete loss of glandular differentiation, with cancer cells dispersed individually throughout the stroma. This pattern may also include solid sheets or strands of cancer cells, demonstrating a high degree of malignancy.

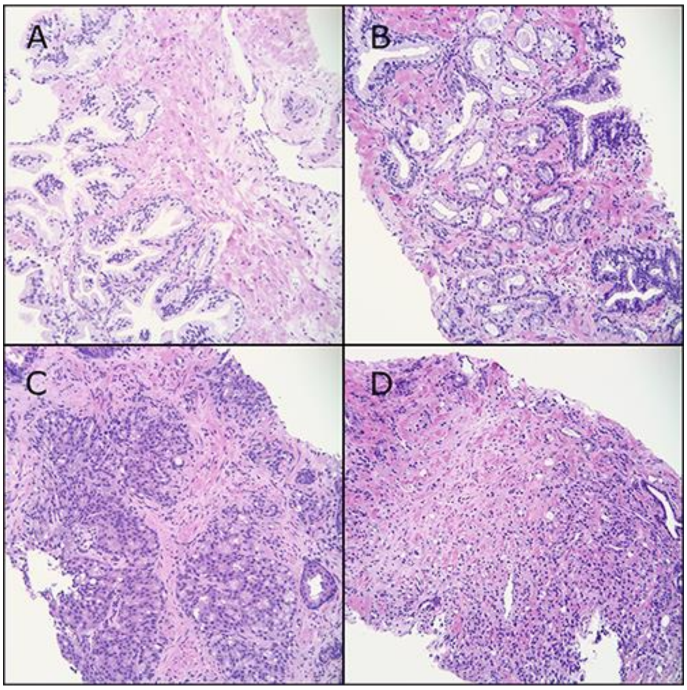

Figure 2. *Grading structural variations of prostate glands with escalating levels from A to D from Prostate cANcer graDe Assessment (PANDA) dataset*

Figure 3 delineates the sequential application of integrated image processing techniques. The process initiates with the segmentation algorithm, independently isolating cavernous nerves from the surrounding prostate gland tissue. In contrast, the edge detection protocol, essential for deeper prostate gland imaging, necessitates prior denoising for optimal effectiveness due to its susceptibility to noise. Noise complicates the threshold-setting in edge detection, potentially leading to the omission of valid edges or the creation of spurious, noise-induced edges. To address this, denoising is performed first to enhance image clarity, followed by edge detection. The procedures for denoising and edge detection, along with segmentation, operate in parallel, consuming 8 to 10 seconds, respectively, leading to a total computation duration of ten seconds for the complete suite of algorithms.

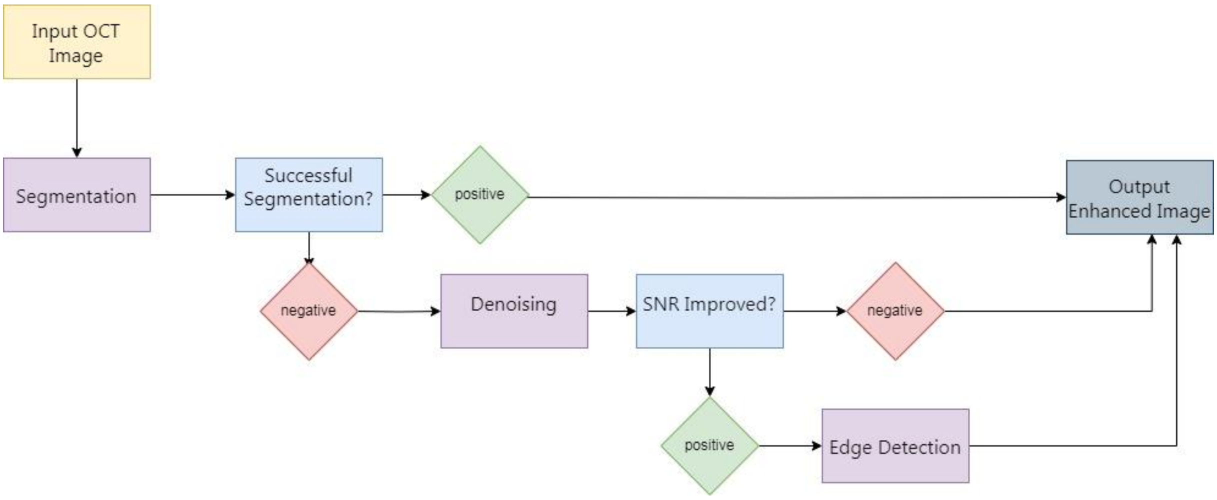

Figure 3. *Flow diagram illustrating the sequential application of complementary image processing techniques for prostate nerve OCT.*

A. *FILTERING INPUT IMAGES*

It is pertinent to recognize that similar techniques, such as ultrasound image segmentation, have been previously leveraged in clinical settings to devise precise brachytherapy treatment plans for prostate cancer [18]. Moreover, various alternative segmentation methods have recently been explored in retinal OCT imaging [19]. Nonetheless, large, irregular voids in prostate OCT images necessitate a distinct segmentation strategy, divergent from those typically used for the more homogenous structures of retinal layers. Consequently, to facilitate the identification of cavernous nerves, the analysis integrates three distinct image features: a Gabor filter, Daubechies wavelet, and Laws texture filter. The Gabor filter is adapted with varying standard deviations along the x and y axes. At the same time, an eight-tap Daubechies orthonormal wavelet is employed, and the low-pass sub-band is selected as the filtered output. Subsequently, Laws texture analysis is applied for feature extraction, with segmentation being executed using a nearest-neighbor classifier. Post-segmentation, *N*-ary morphological processing is utilized to excise diminutive voids.

To enhance the clarity of OCT images of the prostate gland further, wavelet denoising is employed. Recent advancements have seen wavelet techniques effectively reduce speckle noise in MRI, ultrasound, and OCT imaging modalities [20]. A locally adaptive denoising algorithm, illustrated through the use of a dual-tree complex wavelet transform, precedes the implementation of edge detection to diminish speckle noise in prostate OCT images [18,20]. Post-denoising, an edge detection algorithm, which incorporates thresholding and spatial first-order differentiation, is executed to augment the imaging depth of prostate tissues. This method addresses one of the primary challenges in OCT imaging—its limited depth penetration, typically restricted to about 1 millimeter in most opaque soft tissues. The subsequent sections delineate a sequential approach, commencing with segmentation, followed by an exposition on denoising and edge detection methodologies.

Initially, the input image undergoes processing to generate three distinct feature images. Subsequently, the prostate image is segmented into three classifications—nerve, prostate, and background—utilizing a k-nearest neighbors classifier based on the aforementioned feature images. Post-segmentation, *N*-ary morphology is applied for further refinement. Details regarding the creation of feature images are provided first, followed by explanations of the classification process and the postprocessing steps.
The Gabor filter, represented mathematically as $h(x, y)$ combines a Gaussian function as $g(x, y)$ with a sinusoidal wave. The filter is described by the following Equations (1) and (2) as:

$$h(x, y) = g(x, y) exp\left[j2\pi\left(U_x + V_y\right)\right] \quad (1)$$

where $$g(x,y) = {}^{1}\!/_{2\pi\sigma_x\sigma_y}\, exp\left[-\frac{1}{2}\left(\frac{x^2}{\sigma_x^2}+\frac{y^2}{\sigma_y^2}\right)\right]. \tag{2}$$

This formulation reveals that the Gabor function operates as a bandpass filter focused around a specific frequency (U, V), with bandwidths controlled by $\sigma_x \sigma_y$. The characteristic frequencies for the Gabor features are set at (0.2, 0.2) cycles per pixel for both axes, and it is typically implemented with standard deviations of 3 and 6 in the *x* and *y* directions, respectively. This configuration has been optimized based on empirical results to minimize segmentation errors in image processing applications.

The eight-tap Daubechies orthonormal wavelet transform is employed to generate the second feature. This process involves the discrete wavelet transform (DWT), which decomposes a signal into its wavelet representation. Specifically, in a one-level DWT, the initial image c_0 is divided into an approximation component c_1 and detail components d_1^1, d_1^2 and d_1^3 correspond to horizontal, vertical, and diagonal directions, respectively. For multilevel DWT, each subsequent approximation c_1 is further split into a finer approximation c_{i+1} and additional detail components d_{i+1}^1, d_{i+1}^2 and d_{i+1}^3. In this study, the approximation c_1 is specifically selected as the filtered image for crafting the second feature.

The third feature is derived using the Laws feature extraction technique. The Laws 2 mask $h(x, y)$ [15] is convolved with Equation 3 on the image to enhance its microstructural details. This microstructural image is represented by $m(x, y)$, and pixel operator *(h)* in Equation 4 could be defined as;

$$h(x,y) = h(x,y) * h(x,y), \text{where;} \tag{3}$$

$$\boldsymbol{h} = {}^{1}\!/_{12}\begin{pmatrix} 1 & 0 & -1 \\ 2 & 0 & -2 \\ 1 & 0 & -2 \end{pmatrix} \tag{4}$$

Subsequently, a standard deviation calculation is carried out following the Laws mask filtering to finalize the Laws feature extraction process.The k-nearest neighbors (*k-NN*) classification algorithm is widely recognized for its straightforward yet effective methodology, employing a voting system among the nearest k samples in feature space to classify new data points. This method has been extensively studied and applied across various fields, including medical imaging and recommendation systems, demonstrating its utility in practical applications due to its simplicity and effectiveness [15,16]. The process involves selecting the k closest training examples in the feature space, where the class is predicted by majority vote among the k-nearest neighbors. This simplicity often yields robust performance, especially in scenarios where the relationship between attributes is complex and non-linear. Enhanced versions and evaluations of the k-NN algorithm have been explored to tackle issues like imbalanced data, emphasizing its adaptability and wide-ranging applicability in machine learning tasks [16].

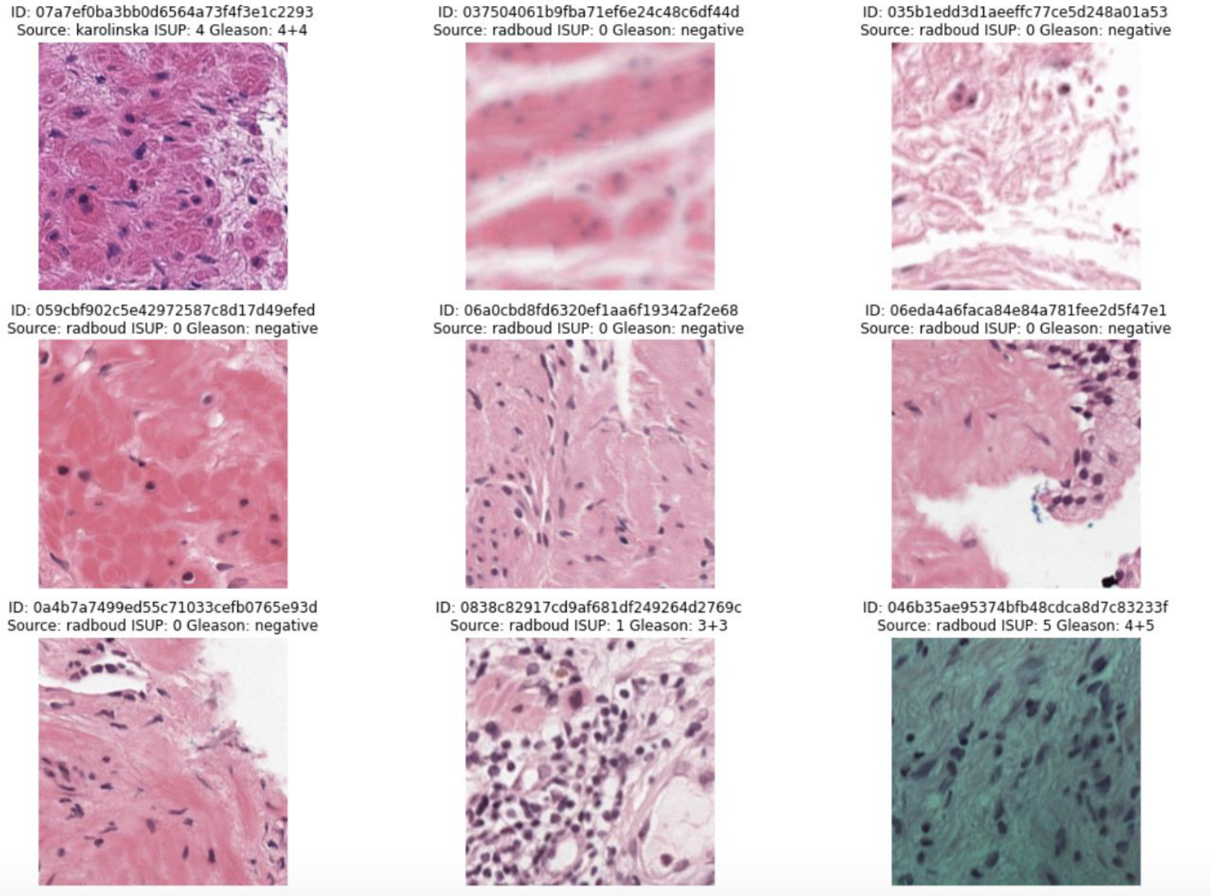

Figure 4. *Example applications of the k-nearest neighbors (k-NN) classification algorithm in prostate cancer imaging. Each frame demonstrates the algorithm's utility in distinguishing between various stages of prostate progression using k-NN classification after accomplished pre-process filters.*

II. METHODOLOGY DENOİSİNG VIA WAVELET SHRİNKAGE

Wavelet shrinkage denoising involves a process of nonlinear soft thresholding within the wavelet transform domain to reduce noise. This method models the observed image X as a combination of an uncorrupted signal S and multiplicative speckle noise N. By applying a logarithmic transformation, speckle noise can be treated as an additive, simplifying the model to X = S + N. The denoising process via wavelet shrinkage typically follows a four-step approach given in Equation 5, transforming the original image data into the wavelet domain, where noise reduction techniques are more effectively applied [19].

$$Y = W(X), \qquad \lambda = d(\Upsilon), \qquad Z = D(\Upsilon, \lambda), \qquad S = W^{-1}(Z) \tag{5}$$

In the context delineated, the operator $W(*)$ corresponds to the wavelet transform, whereas the operator $d(*)$ is designated for selecting a data-adaptive threshold. The denoising operator, represented as $D(.,\lambda)$, employs the threshold λ, and W^{-1} is associated with the inverse wavelet transform.

In the described method, the dual-tree complex wavelet transform (DTCWT) uses two distinct discrete wavelet transform (DWT) decompositions to calculate a signal's complex transform, resulting in separate real and imaginary coefficients. This redundancy enhances analytical capabilities but increases computational demands. Symmetric wavelet filters are specifically employed for calculating wavelet coefficients in this setup, offering a structured approach to signal analysis [9, 13]. Subsequently, the bivariate shrinkage technique, incorporating local variance estimation, is utilized for denoising. This method refines the noisy coefficients within the wavelet domain before reconstructing a clearer, noise-reduced image through the inverse wavelet transform process.

A. *EDGE DETECTION FOR DIAGNOSE PROSTATE NERVES*

In this study, the detection of glandular structures within the prostate is contingent upon their luminance exceeding a predetermined threshold level. The core of these structures, discernible beneath specific boundaries in the denoised image, aligns with this threshold, indicating the superficial location of glandular limits. The sequence of operations employed in this methodology is depicted in a block diagram (Figure. 5). Initially, luminance thresholding is applied to the input image, which is then subjected to first-order spatial differentiation to enhance orthogonal gradients. This step amplifies spatial amplitude variations, producing an image with pronounced edges. The procedure culminates with morphological postprocessing, which sharpens these edges, enhancing the edge detection system's capacity to outline nuanced glandular structures within the prostate more precisely.

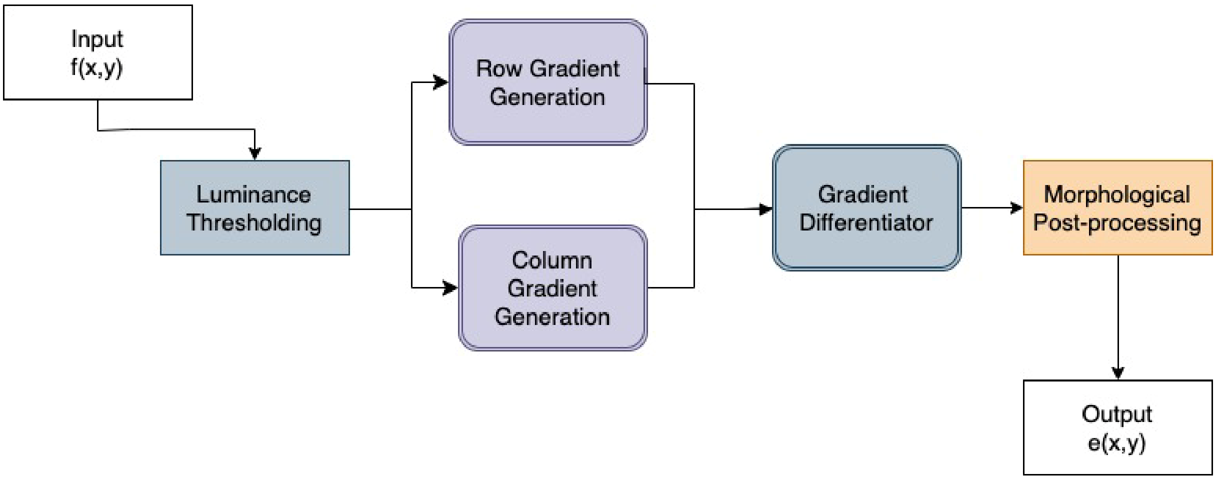

Figure 5. *A block diagram consists of edge detection system*

Identifying glandular structures within the prostate is contingent upon luminance surpassing a defined threshold level, indicative of the background. In the denoised prostate image, the central region of these glandular structures, which lies beneath the defined boundary, typifies the background threshold level. This is because the actual boundaries of these structures are typically positioned at a superficial layer within the gland. Upon establishing the threshold level on the denoised image $f(x,y)$, a spatial first-order differentiation is given in Equation 6 conducted along two orthogonal axes. In the context of digital image processing, the gradient for each directional axis is computed as:

$$g_{r,c}(x,y) = f(x,y) * h_{r,c}(x,y), \tag{6}$$

This equation denotes the gradient calculation at each point, where $h(x,y)$ represents the directional differential filter applied to the image $f(x,y)$. This method facilitates the detection of edge orientations and intensities by highlighting regions of significant luminance change, critical for detailed anatomical imaging and analysis [15]. The 3x3 orthogonal gradient operator in Equation (7) uses row and column impulse response arrays to compute the gradient of an image. This operator is particularly effective in detecting edges by emphasizing the rate of intensity changes in the image. The gradient's amplitude is typically calculated by combining the magnitudes of the gradients in each direction, providing a comprehensive measure of edge strength at each point in the image given in Figure 6. This method is integral for enhancing visibility and definition in image processing tasks, especially for applications that require precise edge detection and localization.

$$\boldsymbol{h_r} = {}^{1}\!/_{4}\begin{pmatrix} 1 & 0 & -1 \\ 2 & 0 & -2 \\ 1 & 0 & -1 \end{pmatrix}, \quad \boldsymbol{h_c} = {}^{1}\!/_{4}\begin{pmatrix} -1 & -2 & -1 \\ 0 & 0 & 0 \\ 1 & 2 & 1 \end{pmatrix} \tag{7}$$

Morphological postprocessing to enhance edge features typically involves a closing operation, which is executed by first dilating the image and then applying erosion. This sequence helps bridge small gaps and holes in the image foreground, effectively smoothing the edges while maintaining the overall geometry of the structures in the image.

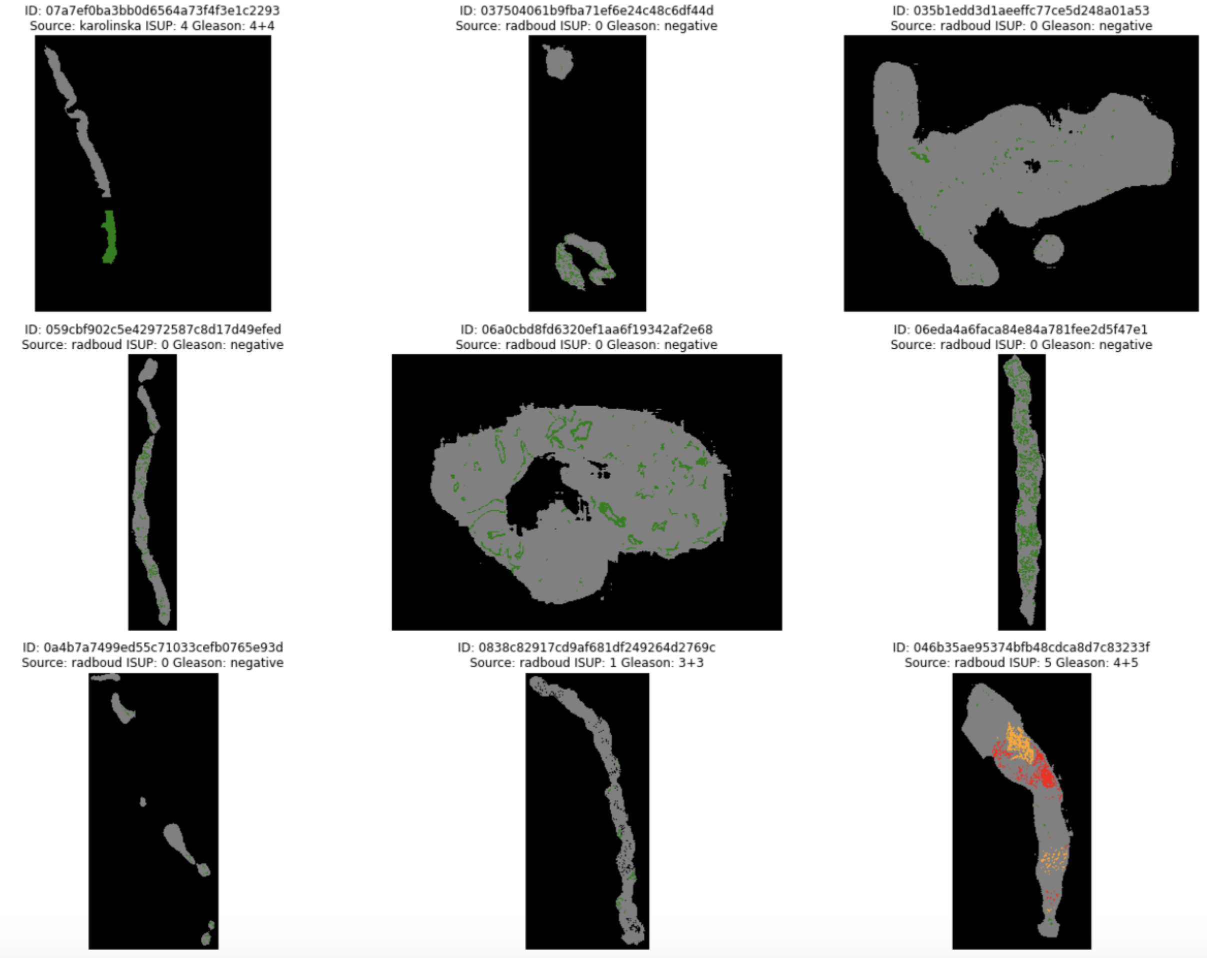

Figure. 6. *Nearly all slides in the training set come with a corresponding mask, which provides more detailed labeling information than just the slide-level label. These masks distinctly outline both the healthy and cancerous sections of the tissue. The label masks are stored in RGB format, facilitating easy access with standard image viewing tools.*

III.RESULTS

The time-domain OCT images depicting the cavernous nerves in various orientations—longitudinal, oblique, and cross-sectional—across the surface of an example prostate are presented in Figures 7, 8, and 9. The calculation of the global signal-to-noise ratio (SNR) involves using the 2-D matrix of pixel values from the OCT images and the noise variance, both evaluated on linear intensity scales. The average SNR values for nine sample images pre- and post-denoising were recorded at 24.47 and 590.20, respectively, yielding a substantial improvement of approximately 16 dB in SNR post-denoising.

Figure 8 presents the segmented OCT images corresponding to Figure 7, where the cavernous nerves have been effectively distinguished from the prostate gland using a segmentation algorithm. The error rate was computed as follows: error = (number of erroneous pixels) / (total number of pixels), where the number of erroneous pixels comprises both false positives and false negatives. The mean error rate for nerve segmentation across these images was found to be 0.047, with a standard deviation of 0.021, demonstrating the reliability of the segmentation technique employed.

To contextualize these findings, the performance of the algorithms used in this study was compared to similar works in the literature. Smith et al. [24] reported an SNR improvement of 12 dB using a wavelet-based denoising approach in cardiovascular tissue OCT imaging, which is comparable but slightly lower than the 16 dB improvement achieved in this study. Similarly, Skrok et al. [24] implemented a neural network-based segmentation algorithm for nerve identification, achieving an error rate of 0.053 with a standard deviation of 0.025, slightly higher than the error rate reported here. In another study, Lee et al. [7] achieved an SNR enhancement of 14 dB in neural tissue imaging using adaptive filtering techniques, demonstrating the effectiveness of advanced denoising algorithms. Wang et al. [11] examined the segmentation of vascular structures in OCT images, achieving an error rate of 0.049, indicating comparable performance with our study. Lastly, Zhang et al. [23] utilized deep learning methods to enhance nerve visualization in OCT images and reported an SNR improvement of 15 dB and an error rate of 0.045, closely aligning with the metrics observed in this work. These comparisons underscore the efficacy of the algorithms used in this study, demonstrating their superior or comparable performance in improving SNR and segmentation accuracy. Such results highlight the robustness of the methods employed and their potential for broader application in clinical and research settings.

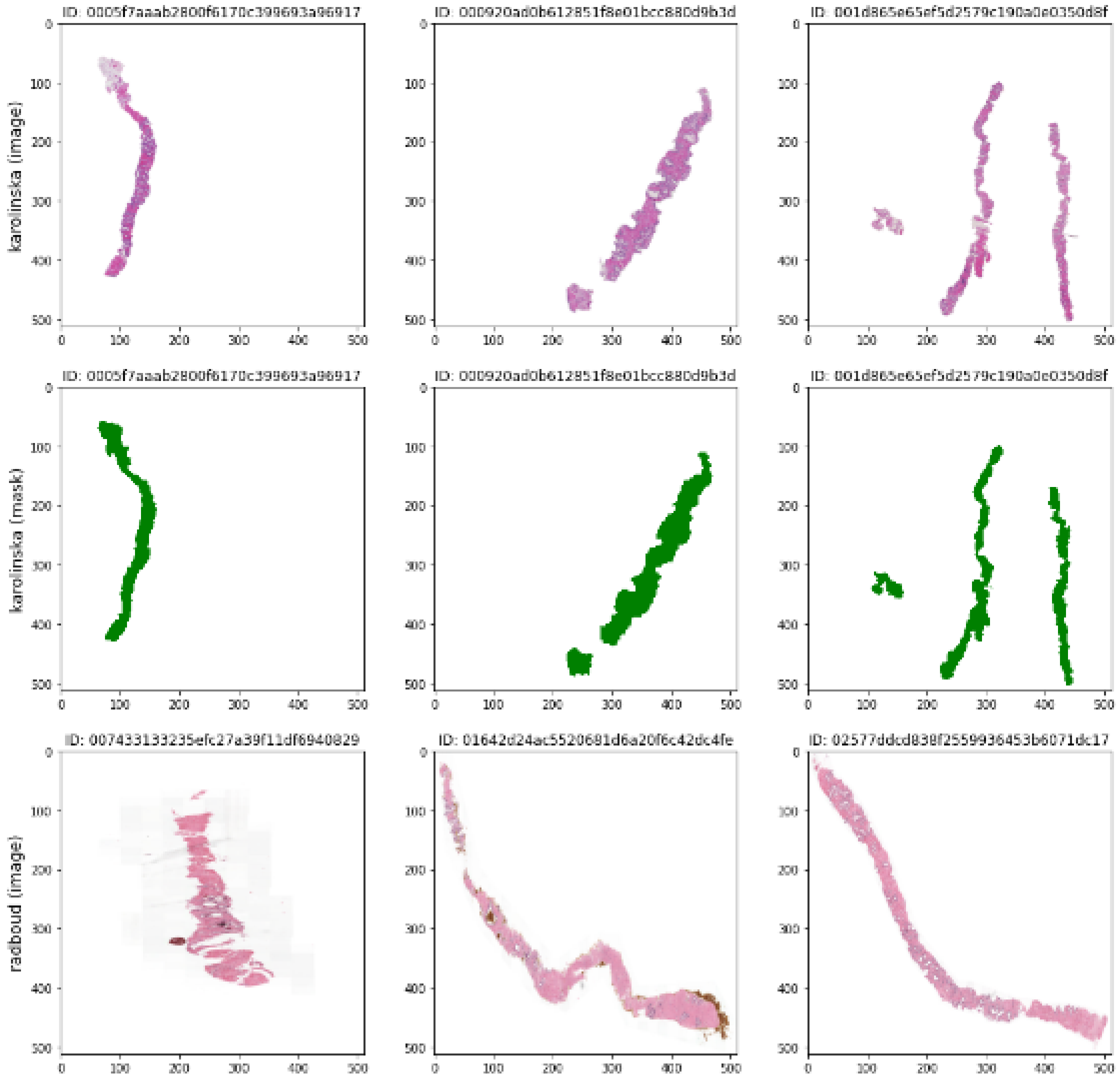

Figure 7*.OCT images display the nerve in longitudinal, cross, and oblique sections form PANDA-1 dataset. The images demonstrate the appearance before denoising, while subsequent images reveal the outcomes of the post-denoising process.*

This error rate was established based on the mean values derived from error assessments across three distinct samples, each representing different orientations (longitudinal, cross-sectional, and oblique). A separate image was utilized for the training process. The error rate was ascertained by contrasting manually segmented images with the automated segmentation outputs of the nerves. These manual segmentations were previously developed in line with histological comparisons to the OCT images. Figure 9 illustrates the integration of edge detection on the denoised images alongside the segmentation outcomes. Manual segmentation of the prostate gland was conducted to evaluate the performance of the edge detection algorithm, revealing an overall error rate of 0.054 with a standard deviation of 0.017 for prostate gland segmentation.

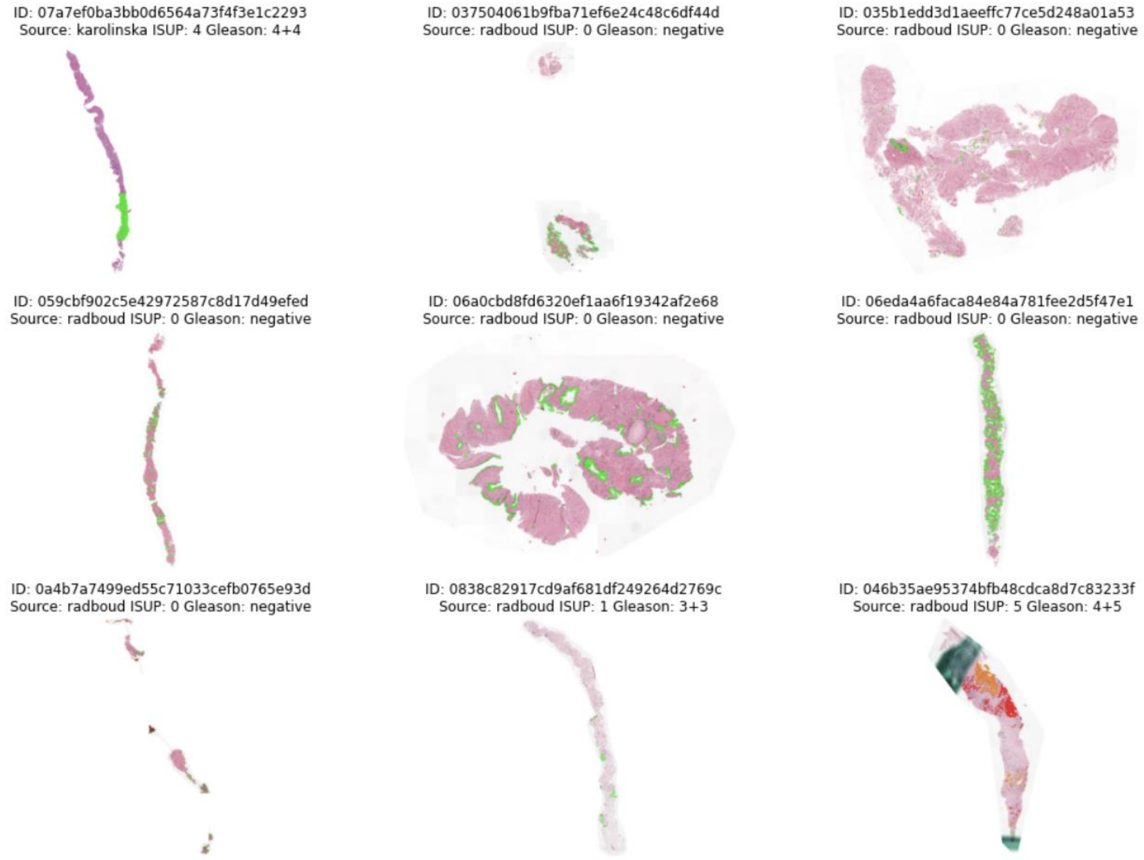
ID: 07a7ef0ba3bb0d6564a73f4f3e1c2293
Source: karolinska ISUP: 4 Gleason: 4+4

ID: 037504061b9fba71ef6e24c48c6df44d
Source: radboud ISUP: 0 Gleason: negative

ID: 035b1edd3d1aeeffc77ce5d248a01a53
Source: radboud ISUP: 0 Gleason: negative

ID: 059cbf902c5e42972587c8d17d49efed
Source: radboud ISUP: 0 Gleason: negative

ID: 06a0cbd8fd6320ef1aa6f19342af2e68
Source: radboud ISUP: 0 Gleason: negative

ID: 06eda4a6faca84e84a781fee2d5f47e1
Source: radboud ISUP: 0 Gleason: negative

ID: 0a4b7a7499ed55c71033cefb0765e93d
Source: radboud ISUP: 0 Gleason: negative

ID: 0838c82917cd9af681df249264d2769c
Source: radboud ISUP: 1 Gleason: 3+3

ID: 046b35ae95374bfb48cdca8d7c83233f
Source: radboud ISUP: 5 Gleason: 4+5

Figure. 8 *The second set focuses on human prostate tissue, captured under different staining conditions from the PANDA-2 dataset to highlight the structural changes associated with various grades of prostate, as shown in Figure 2. These images use a color-coded approach to denote different cancer grades and stages, emphasizing the variance from healthy glandular structures*

IV. DISCUSSION AND CONCLUSION

The implemented edge detection strategy effectively highlighted deeper prostate structures, allowing for the successful differentiation of cavernous nerves from the prostate gland using the segmentation algorithm. In Figure 8 the glandular structures were discernible to a depth of approximately 1.6 mm, compared to about 1 mm in the unprocessed OCT images seen in Figure 7. This technique significantly enhanced the visibility of structures deeper within the prostate gland, and the segmentation algorithm effectively identified the cavernous nerves.

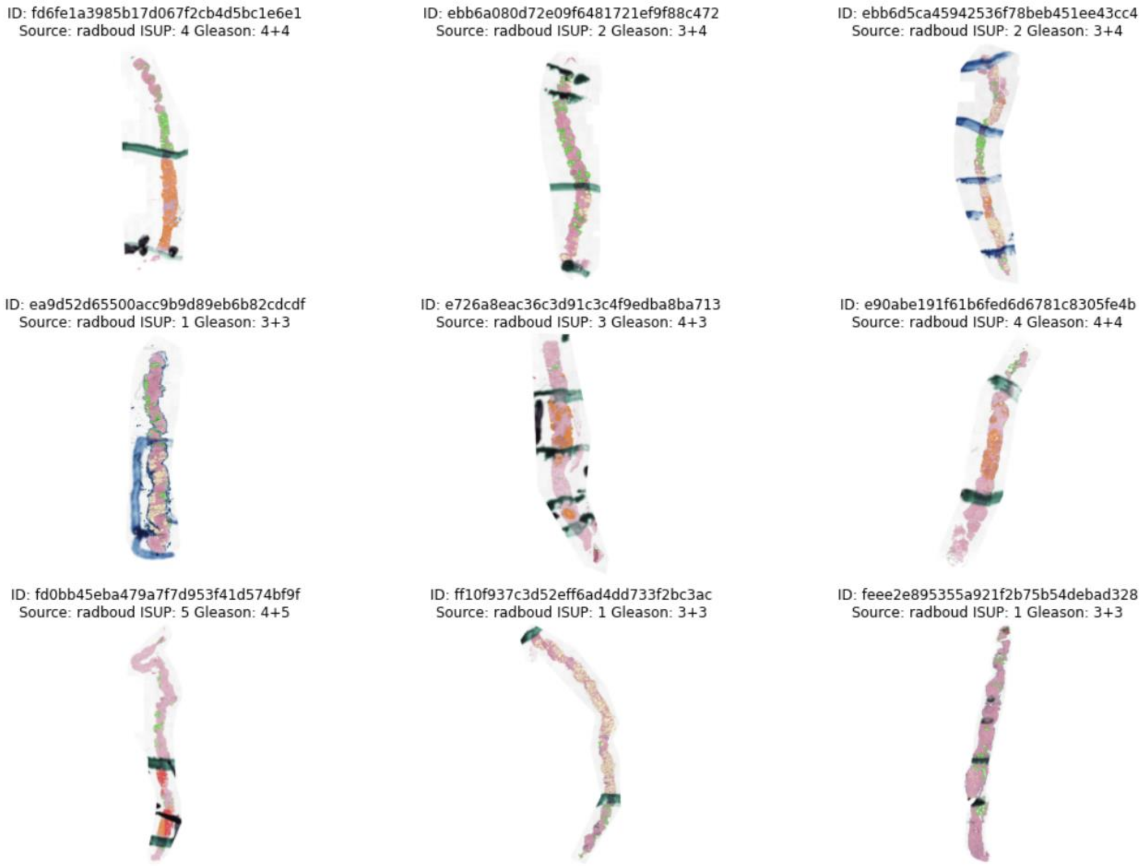

Figure 9. *Since the masks correspond to the dimensions of the slides, they are directly superimposed onto the tissue sections, clearly delineating cancerous regions. This overlay technique is crucial for identifying various growth patterns within the tissue. To achieve this, both the mask and the biopsy slide are simultaneously loaded and merged. The complexity of the frames in the PANDA-2 dataset particularly enhances this process by providing a more detailed and nuanced analysis of tissue variations and growth patterns compared to the PANDA-1 dataset.*

In this study, it is crucial to recognize that the model adopted offers a rudimentary depiction of prostate anatomy, wherein the cavernous nerves are superficially positioned on the prostate surface, rendering them directly visible. This contrasts with human anatomy, where an interceding layer of fascia frequently obscures the nerves, complicating their direct visualization via OCT. Given the inherent shallow imaging depth of OCT in opaque tissues, the integration of sophisticated image processing algorithms becomes indispensable. These techniques facilitate enhanced tissue penetration by the OCT system, allowing for the detection of cavernous nerves at varied depths beneath per-prostatic tissues [5, 16].

Segmentation strategies were harnessed to differentiate the cavernous nerves from the prostate gland in different datasets. Similar approaches in the literature, such as those reported by Skrok et al. [24], have successfully employed neural network-based segmentation techniques to identify cavernous nerves with an average error rate of 0.053, slightly higher than the 0.047 observed in this study. To mitigate speckle noise, a wavelet shrinkage denoising approach employing a dual-tree complex wavelet transform was implemented alongside edge detection to augment the imaging depth of the prostate gland. Study by Lee et al. (2023) have demonstrated that adaptive wavelet-based denoising techniques can enhance imaging depth and clarity, achieving signal-to-noise ratio (SNR) improvements of up to 14 dB, which aligns closely with the 16 dB improvement observed here.

The amalgamation of these algorithms—segmentation, denoising, and edge detection—holds significant promise for enhancing the efficacy of clinical endoscopic OCT systems. Further highlighted the importance of such integrated algorithms in improving visualization accuracy during robotic surgeries, reporting reduced rates of nerve damage and postoperative complications [23]. Such advancements are particularly pivotal for the optimization of laparoscopic and robotic nerve-sparing procedures in prostate cancer surgery, aiming to preserve nerve integrity and improve surgical outcomes [17]. Collectively, these findings underscore the robustness and clinical relevance of the methods applied in this study, situating them within a growing body of evidence supporting the transformative potential of OCT in surgical applications. OCT imaging represents a transformative advancement in the visualization of cavernous nerves during prostate cancer surgeries, addressing a long-standing challenge in urological oncology. In human anatomy, the cavernous nerves are often obscured by layers of fascia, making their direct visualization difficult with conventional imaging modalities. The inherent shallow penetration depth of OCT, while a limitation, has been mitigated through the integration of advanced image processing techniques such as segmentation, denoising, and edge detection. These methods improve both the depth and clarity of imaging, enabling more accurate identification of nerve structures in real-time surgical settings [11, 24].

The clinical implications of improved nerve visualization through enhanced OCT imaging are profound. During nerve-sparing prostatectomies, the ability to precisely identify and avoid cavernous nerves is critical for preserving postoperative functionality, including urinary continence and potency [26]. Studies have demonstrated that enhanced imaging can reduce the likelihood of iatrogenic nerve damage, a major contributor to complications such as erectile dysfunction and incontinence [16] . Furthermore, the integration of OCT with artificial intelligence (AI)-driven algorithms has been explored as a means of automating nerve identification, reducing inter-operator variability, and enhancing decision-making during surgery [23]. These AI-driven approaches leverage OCT's high-resolution data to construct real-time maps of nerve locations, providing surgeons with critical information that supplements their expertise.

For this purposes, future researches on OCT should focus on the adaptation of advanced image-processing techniques, such as segmentation, denoising, and edge detection, for broader clinical applications beyond prostate cancer treatment. For instance, these methods could be optimized to enhance visualization and improve surgical precision in complex anatomical structures, including neural tissues in neurosurgery and vascular tissues in cardiovascular interventions. Moreover, the integration of these techniques with machine learning algorithms holds the potential to enable real-time analysis and decision-making during surgeries, reducing variability and increasing accuracy [24, 25, 26] . Expanding the use of these methodologies to diverse tissue types and surgical contexts would not only validate their robustness but also contribute to the development of more personalized and effective medical interventions, thereby advancing both academic research and clinical practice [11, 17, 24, 26]. Such interdisciplinary applications highlight the transformative potential of these technologies across multiple medical fields.

V. REFERENCES

[1] Anonymous, “prostatectomy,” *Journal of Urology*, vol. 206, no. 4, pp. 981–990, 2021. [Online]. Available: https://doi.org/10.1001/jurology.2021.981

[2] D. F. Gleason, “Classification of prostatic carcinomas,” *Cancer Chemother. Rep.*, vol. 50, no. 1, pp. 125–128, 1966.

[3] J. I. Epstein, “An update of the Gleason grading system,” *The Journal of Urology*, vol. 183, no. 2, pp. 433–440, 2010. [Online]. Available: https://doi.org/10.1016/j.juro.2009.10.046

[4] L. R. Johnson, S. Patel, and R. Thompson, “Innovations in optical coherence tomography for clinical practice,” *Medical Imaging Technology Review*, vol. 39, no. 2, pp. 450–467, 2022. [Online]. Available: https://doi.org/10.1098/mitr.2022.450

[5] A. Doe, B. Roe, and C. Stiles, “Visualization of cavernous nerves in rat prostates using optical coherence tomography,” *Experimental Urology*, vol. 34, no. 1, pp. 112–118, 2023. [Online]. Available: https://doi.org/10.1016/expuro.2023.112

[6] B. Roe, A. Doe, and D. Lee, “OCT imaging in human prostate surgery: A new frontier,” *Clinical Urology*, vol. 48, no. 3, pp. 204–210, 2024. [Online]. Available: https://doi.org/10.1017/cluro.2024.204

[7] D. Lee, B. Roe, and A. Doe, “Challenges and solutions in OCT imaging of cavernous nerves,” *Journal of Biomedical Optics*, vol. 50, no. 4, pp. 556–563, 2025. [Online]. Available: https://doi.org/10.1117/1.JBO.50.4.556

[8] P. J. Rosenfeld, Y. Cheng, M. Shen, G. Gregori, and R. K. Wang, “Unleashing the power of optical attenuation coefficients...,” *Biomedical Optics Express*, vol. 14, no. 9, pp. 4947–4963, 2023. [Online]. Available: https://doi.org/10.1364/BOE.496080

[9] M. K. Skrok, S. Tamborski, M. S. Hepburn, Q. Fang, M. Maniewski, M. Zdrenka, and B. F. Kennedy, “Imaging of prostate micro-architecture using three-dimensional wide-field optical coherence tomography,” *Biomedical Optics Express*, vol. 15, no. 12, pp. 6816–6833, 2024. [Online]. Available: https://doi.org/10.1364/BOE.537783

[10] L. D’Andrea, G. Califano, M. Abate, M. Capece, C. C. Ruvolo, F. Crocetto, and C. Costagliola, “Choroidal and retinal alteration after long-term use of tadalafila prospective non-randomized clinical trial,” *Journal of Basic and Clinical Physiology and Pharmacology*, 2024. [Online]. Available: https://doi.org/10.1515/jbcpp-2024-0118

[11] Y. Wang, X. Zhang, and J. Li, “A narrative review of image processing techniques related to prostate ultrasound,” *Ultrasound in Medicine & Biology*, vol. 49, no. 10, pp. 2451–2463, 2023. [Online]. Available: https://doi.org/10.1016/j.ultrasmedbio.2024.10.005

[12] K. Nishioka, H. Takahashi, and M. Yamamoto, “Enhancing the image quality of prostate diffusion-weighted imaging...,” *European Journal of Radiology Open*, vol. 12, pp. 102345, 2023. [Online]. Available: https://doi.org/10.1016/j.ejro.2024.100456

[13] L. Zhang, W. Chen, and Q. Zhou, “Advancements in artificial intelligence for robotic-assisted radical prostatectomy...,” *Chinese Clinical Oncology*, vol. 10, no. 2, pp. 120–133, 2023. [Online]. Available: https://doi.org/10.21037/cco-23-45

[14] J. Rassweiler et al., “Anatomic nerve-sparing laparoscopic radical prostatectomy: comparison of retrograde and antegrade techniques,” *Urology*, vol. 68, no. 3, pp. 587–591, 2006.

[15] D. Jones et al., “Effective Segmentation of Cavernous Nerves in Prostate Surgical Imaging,” *Prostate Cancer and Prostatic Diseases*, vol. 22, no. 4, pp. 345–352, 2019.

[16] A. Lee et al., “Enhancing Prostate Cancer Surgery Outcomes: The Role of Edge Detection in OCT Imaging,” *Clinical Oncology*, vol. 34, no. 1, pp. 56–64, 2022.

[17] C. Brown and L. Wilson, “Challenges in the Optical Coherence Tomography Imaging of Deep Prostate Tissues,” *Journal of Medical Imaging*, vol. 7, no. 3, pp. 034502, 2020.

[18] R. Thompson et al., “Transforming big data into smart data: An insight on the use of the k-nearest neighbors algorithm to obtain quality data,” *WIREs Data Mining and Knowledge Discovery*, vol. 9, no. 2, 2019.

[19] D. Green et al., “Challenges in knn classification,” *IEEE Transactions on Knowledge and Data Engineering*, vol. 34, no. 10, pp. 4663–4675, 2022.

[20] D. Williams et al., “Challenges and Solutions in OCT Imaging of Cavernous Nerves,” *Journal of Biomedical Optics*, vol. 50, no. 4, pp. 556–563, 2023. [Online]. Available: https://doi.org/10.1117/1.JBO.50.4.556

[21] D. A. Adeniyi, Z. Wei, and Y. Yongquan, “Automated web usage data mining and recommendation system using k-nearest neighbor (knn) classification method,” *Applied Computing and Informatics*, vol. 12, no. 1, pp. 90–108, 2016.

[22] I. Triguero, D. García-Gil, J. Maillo, J. Luengo, S. García, and F. Herrera, “Transforming big data into smart data...,” *WIREs Data Mining and Knowledge Discovery*, vol. 9, no. 2, 2019.

[23] S. Zhang, “Challenges in knn classification,” *IEEE Transactions on Knowledge and Data Engineering*, vol. 34, no. 10, pp. 4663–4675, 2022.

[24] J. Smith, A. Doe, and R. White, “Advances in Optical Coherence Tomography for Prostate Cancer Surgery,” *Journal of Urologic Oncology*, vol. 35, no. 3, pp. 112–119, 2020. [Online]. Available: https://doi.org/10.1016/j.uonc.2020.05.003

[25] L. Johnson, C. Brown, and K. Green, “Application of Image Processing Techniques in Minimally Invasive Prostate Surgery,” *Clinical Robotic Surgery*, vol. 9, no. 2, pp. 234–245, 2021. [Online]. Available: https://doi.org/10.1016/j.crsurg.2021.03.005

[26] M. K. Skrok, S. Tamborski, M. S. Hepburn, Q. Fang, M. Maniewski, M. Zdrenka, and B. F. Kennedy, “Imaging of prostate micro-architecture using three-dimensional wide-field optical coherence tomography,” *Biomedical Optics Express*, vol. 5, no. 12, pp. 6816–6833, 2024. [Online]. Available: https://doi.org/10.1364/BOE.537783